

A transient multi-scale model for direct methanol fuel cells

T. Jahnke^{1,*}, M. Zago², A. Casalegno², W. G. Bessler³, A. Latz^{1,4}

¹German Aerospace Center (DLR), Institute of Technical Thermodynamics, Pfaffenwaldring
38-40, 70569 Stuttgart, Germany,

²Politecnico di Milano, Department of Energy, via Lambruschini 4, 20156 Milano, Italy

³Institute of Energy System Technology (INES), Offenburg University of Applied Sciences,
Badstrasse 24, 77652 Offenburg, Germany

⁴Helmholtz Institute Ulm for Electrochemical Energy Storage (HIU), Helmholtzstraße 11,
89081 Ulm, Germany

* Corresponding author. E-mail address: thomas.jahnke@dlr.de

ABSTRACT

The DMFC is a promising option for backup power systems and for the power supply of portable devices. However, from the modeling point of view liquid-feed DMFC are challenging systems due to the complex electrochemistry, the inherent two-phase transport and the effect of methanol crossover. In this paper we present a physical 1D cell model to describe the relevant processes for DMFC performance ranging from electrochemistry on the surface of the catalyst up to transport on the cell level. A two-phase flow model is implemented describing the transport in gas diffusion layer and catalyst layer at the anode side. Electrochemistry is described by elementary steps for the reactions occurring at anode and cathode, including adsorbed intermediate species on the platinum and ruthenium

surfaces. Furthermore, a detailed membrane model including methanol crossover is employed. The model is validated using polarization curves, methanol crossover measurements and impedance spectra. It permits to analyze both steady-state and transient behavior with a high level of predictive capabilities. Steady-state simulations are used to investigate the open circuit voltage as well as the overpotentials of anode, cathode and electrolyte. Finally, the transient behavior after current interruption is studied in detail.

Keywords: Direct methanol fuel cell (DMFC), modeling, performance, transient.

1. INTRODUCTION

Direct methanol fuel cell (DMFC) technology is promising as a power source for portable and uninterruptible power supply applications, due to the direct use of a high energy density liquid fuel, quick recharging by refilling and low operating temperature[1,2].

However, the use of a methanol/water liquid mixture as fuel, as required by electrochemistry, increases the complexity of the system and entails some additional challenges:

- a complex two-phase and multi-component flow has to be managed at the anode side;
- the methanol oxidation is a complex multi-step mechanism leading to a strong CO poisoning of the platinum catalyst: to improve the capability of methanol oxidation platinum-ruthenium catalysts are used for DMFC anodes;
- methanol permeates through the membrane and the resulting methanol oxidation at the cathode side leads to waste of fuel and significantly affects cathode potential, forming a so called mixed potential.

In addition, other technical issues must still be overcome to enter into the market, among which is the severe performance degradation over operation time. DMFC performance losses

show a permanent and a temporary contribution at both anode and cathode[3-5]. The former is due to irreversible degradation mechanisms, such as platinum dissolution and agglomeration at the cathode, while the latter is partially recovered by utilizing appropriate operating strategies[6]. Usually these strategies consist of a period of continuous operation interspersed by a sequence of OCV and/or cathode air feeding interruption.

Current research activities aim at studying DMFC transient behavior to improve and consolidate the understanding of system operation and to set the basis for reducing DMFC degradation. Due to the complex and nonlinearly-coupled processes taking place in DMFCs, modeling and simulation are highly useful tools [7-12].

Wang and Wang[7] presented a two-phase model, taking into account the effect of methanol crossover, but considering only global reactions for methanol oxidation reaction (MOR) and oxygen reduction reaction, i.e., did not take into account the effect of CO poisoning.

Siebke et al.[8] developed a DMFC model, in which a multi-step mechanism for the MOR is considered at the anode side while at the cathode MOR and oxygen reduction reaction (ORR) are modeled using Tafel equations. The model was used to investigate the limiting processes at high current densities depending on the operating conditions.

Casalegno et al. considered a 1D+1D steady-state model including two-phase transport, where the reaction kinetics of MOR and ORR is given by Tafel equations and validated the model for a wide range of operating conditions and with diffusion layer configurations [9].

Gerteisen[10] presented a multi-step model for MOR and ORR including oxygen bleeding to remove the CO poisoning at the cathode. The model was used to discuss transient effects, e.g., the dynamics of CO poisoning after current interruption. However, the model did not include two-phase transport.

Kulikovsky[11] developed an analytical model for cathode mixed potential based on Butler-Volmer kinetics of the ORR.

From the modeling point of view, only very limited work has been carried out concerning the simulation and experimental validation of both DMFC steady-state and dynamic behavior, that is fundamental to couple performance and degradation models [13].

Hence, the aim of this work is to develop a physical DMFC model which is capable of describing the performance of DMFC during steady-state as well as transient operation. In this paper we first present a detailed cell model based on the in-house modeling framework DENIS[14,15] which provides several models for high and low temperature fuel cells as well as different types of batteries. This framework has been complemented by the DMFC model presented in this paper by including the relevant mechanisms mentioned before, i.e., two-phase-flow, a multi-step mechanism for the methanol oxidation as well as methanol crossover and multi-step MOR and ORR at the cathode. All implemented model equations are presented in the first part of this paper. Next, we show validation of the model with respect to different experimental measurements, i.e., polarization curves, methanol crossover measurements and electrochemical impedance spectra. Finally, after validation, the relevance of the different mechanisms on the cell performance and on the transient behavior of the cell is discussed. In particular, the effects of current interruption are investigated.

2. MODEL

In the following we describe the developed DMFC model including all model equations and parameters. A 1D continuum approach is used to model the Membrane Electrode Assembly (MEA). The model is isothermal and is composed of several sub-models for the different components (gas diffusion layers (GDLs), catalyst layers (CLs) and membrane (MEM)). The different domains are spatially resolved in through plane direction, i.e., gradients along the

channel are neglected. This assumption is justified for sufficiently high stoichiometries which are considered in the model validation experiments. For low stoichiometries gradients along the channel might become important. This would require the description by a 2D model, which is beyond the scope of this work. In the following sections, the model equations used to describe all physical processes in the different layers are introduced and the boundary conditions are presented in Section 2.3. Symbols are defined in the nomenclature Table. The model parameters (e.g. thicknesses of the components, transport parameters, etc.) are listed in Table 4. The simulation methodology is described in Section 2.6.

2.1. Transport in gas diffusion layers and catalyst layers

Within the porous electrode at the anode side, we consider a two-phase transport model[16]. The governing equations for the mass transport in GDL and CL are formally identical. Both layers differ only with respect to parameters like the volume fractions of the respective bulk phases, porosity, PTFE-loading etc.

The species conservation in the gas phase is given by[14]

$$\frac{\partial(\varepsilon^g c_i^g)}{\partial t} = -\frac{\partial J_i^{g, \text{diff}}}{\partial y} - \frac{\partial J_i^{g, \text{conv}}}{\partial y} + \sum_k A_k^V \dot{s}_i^k, \quad (1)$$

where the diffusive flux is described in implicit form by the Stefan-Maxwell law

$$\frac{\partial(\varepsilon^g c_i^g)}{\partial y} = \sum_j \frac{x_i J_j^{g, \text{diff}} - x_j J_i^{g, \text{diff}}}{D_{ij}^{\text{eff}}} \quad (2)$$

and the pressure driven Darcy flow is given by

$$J_i^{\text{g,conv}} = -c_i^{\text{g}} \frac{k^{\text{g}}}{\mu^{\text{g}}} \frac{\partial p^{\text{g}}}{\partial y} , \quad (3)$$

where μ^{g} is the mean gas viscosity and k^{g} is the permeability of the gas phase.

In the chemical source term A_k^V denotes the volume-specific surface area of surface k and \dot{s}_i^A is the corresponding surface chemical reaction rate of species i . Note, that also in the GDL we can have such a source term for methanol and water due to the phase transition between liquid phase and gas phase (see below).

For the cathode side, we consider the gas phase only, i.e., equations (1)-(3) are sufficient to describe the transport behavior, as long as flooding phenomena are not taken into account. However, since liquid methanol-water mixture enters the anode and gaseous CO_2 leaves through the channel, it is crucial to use a two-phase model at the anode side.

In this case, the governing equations for the liquid-phase transport are very similar to those of the gas phase. Species conservation again includes diffusion, convection and chemical source terms

$$\frac{\partial(\varepsilon^{\text{l}} \rho_i^{\text{l}})}{\partial t} = -\frac{\partial j_i^{\text{l,diff}}}{\partial y} - \frac{\partial j_i^{\text{l,conv}}}{\partial y} + \sum_k A_k^V \dot{s}_i^k M_i . \quad (4)$$

We assume Fickian diffusion within the liquid phase

$$j_i^{\text{l,diff}} = -D_i^{\text{l}} \frac{\partial \rho_i^{\text{l}}}{\partial y} . \quad (5)$$

The convective flux is determined by the liquid pressure gradient within the GDL/CL according to

$$j_i^{\text{l,conv}} = v^{\text{conv}} \rho_i^{\text{l}} , \quad (6)$$

with the convection velocity

$$v^{\text{conv}} = -\frac{k^l}{\mu^l} \frac{\partial p^l}{\partial y} \quad (7)$$

Here μ^l denotes the viscosity and k^l the permeability of the liquid phase.

The temperature dependent viscosity is taken to be similar to pure water and described by[17]

$$\mu^l = 10^{-3} \frac{(T-273.15) + 246}{0.05594 (T-273.15)^2 + 5.2842 (T-273.15) + 137.37} \quad (8)$$

The permeabilities k^l and k^g are calculated as the product of relative and absolute permeability

$$k^p = k_{\text{rel}}^p k_{\text{abs}} \quad (9)$$

The relative permeabilities[18] depend on the liquid saturation $s = \varepsilon^l / \varepsilon$ and are calculated as

$$k_{\text{rel}}^l = s^{3.5}, \quad k_{\text{rel}}^g = (1-s)^{3.5} \quad (10)$$

whereas the absolute permeability follows from the Kozeny-Carman relationship[19]

$$k_{\text{abs}} = \frac{\varepsilon^3 d_p^2}{72\tau(1-\varepsilon)^2} \quad (11)$$

The pressure of liquid phase and gas phase are connected with each other by the capillary pressure $p^c = p^l - p^g$, which is described by a Leverett function according to

$$p_c = \gamma \sqrt{\frac{\varepsilon}{k^l}} J(s) \quad (12)$$

We fitted this Leverett function based on the experimental data of Hao and Cheng[20] and obtained

$$J(s) = 0.18 + 0.00498\exp(10.5(s - 0.5)) - 0.00397\exp(-11.19(s - 0.5)) . \quad (13)$$

The surface tension of water against air is calculated as[16]

$$\gamma = -1.78 \cdot 10^{-4}T + 0.1247 . \quad (14)$$

Equation (4) is solved with respect to the variables $\rho_i^{\text{liquid}} = \varepsilon^{\text{liquid}} \rho_i^{\text{pore}}$. From these densities the volume fraction of the liquid mixture can be calculated as

$$\varepsilon^{\text{liquid}} = \sum_i V_i^{\text{liquid}} \rho_i^{\text{liquid}} / M_i , \quad (15)$$

with the respective partial molar volumes V_i^{liquid} in the liquid phase.

Both, methanol and water can undergo a phase transition from liquid to gas phase according to



For the kinetics of these phase transitions we apply the Hertz-Knudsen equation[15,21]. The net rate of evaporation is given by

$$\dot{s}_i^{\text{evap,net}} = \dot{s}_i^{\text{evap}} - \dot{s}_i^{\text{cond}} = \alpha \frac{p_{i,0}(T) - p_i^g}{\sqrt{2\pi M_i RT}} , \quad (18)$$

where $p_{i,0}(T)$ denotes the respective saturation pressure. Using the Clausius-Clapeyron equation, the saturation pressure is related to the enthalpy of evaporation ΔH according to

$$p_{i,0}(T) = p_1 \exp \left[-\frac{\Delta H}{R} \left(\frac{1}{T} - \frac{1}{T_1} \right) \right], \quad (19)$$

where p_1 is the vapor pressure at temperature T_1 .

2.2. Membrane

Within the membrane, water transport is described by means of the water content λ , which is the local number of water molecules per SO_3 site. We assume that the transport of methanol and water through the membrane is driven by diffusion and electro-osmotic drag[9,10].

Therefore, water transport is calculated according to

$$\frac{\partial \lambda}{\partial t} = -\frac{EW}{\rho_{\text{H}_2\text{O}}^{\text{mem}}(\lambda)} \frac{\partial J_{\text{H}_2\text{O}}^{\text{mem}}}{\partial y}, \quad (20)$$

with

$$J_{\text{H}_2\text{O}}^{\text{mem}} = -D_{\text{H}_2\text{O}}^{\text{mem}}(T) \frac{\partial c_{\text{H}_2\text{O}}^{\text{mem}}}{\partial y} - d_{\text{H}_2\text{O}}(\lambda) i / F. \quad (21)$$

Here, the temperature dependent diffusion coefficient is calculated according to the model of Weber and Newman[22]

$$D_{\text{H}_2\text{O}}^{\text{mem}}(T) = 1.8 \cdot 10^{-9} f_v e^{20000/R(1/303.15-1/T)}, \quad (22)$$

where the volume fraction of water in the membrane is defined as

$$f_v = \frac{\lambda \bar{V}_{\text{H}_2\text{O}}}{\bar{V}_{\text{mem}} + \lambda \bar{V}_{\text{H}_2\text{O}}}, \quad (23)$$

with the molar volume of water $\bar{V}_{\text{H}_2\text{O}}$ and the molar volume of the dry membrane \bar{V}_{mem} .

The drag coefficient for water[23] is given as

$$d_{\text{H}_2\text{O}}(\lambda) = 1.0 + 0.028\lambda + 0.0026\lambda^2 \quad . \quad (24)$$

The methanol transport through the membrane is also driven by diffusion and electro-osmotic drag

$$J_{\text{CH}_3\text{OH}}^{\text{mem}} = -D_{\text{CH}_3\text{OH}}^{\text{mem}} \frac{\partial c_{\text{CH}_3\text{OH}}^{\text{mem}}}{\partial y} - d_{\text{CH}_3\text{OH}} i / F \quad , \quad (25)$$

with the drag coefficient $d_{\text{CH}_3\text{OH}} = 2.5x_{\text{CH}_3\text{OH}}^{\text{mem}}$ for methanol[24].

Concerning the ionic transport, the λ -dependent proton conductivity of the membrane is given by[23]

$$\sigma_{\text{mem}} = (0.46\lambda - 0.25) \exp\left[-1190\left(\frac{1}{T} - \frac{1}{298.15}\right)\right] \quad . \quad (26)$$

This expression is used to calculate the potential within the membrane (cf. Sec. 2.4.).

2.3. Boundary conditions

We choose Dirichlet boundary conditions for all species at the channel sides of the GDL.

At the anode side we fix the concentrations of methanol and water in the liquid phase.

For the gas phase at the channel boundary we assume saturation pressure for both methanol and water. Furthermore, we fix the liquid pressure at the channel side of the GDL. Therefore, the capillary pressure at the GDL boundary is determined by

$$p^c \Big|_{y=Lc+Lm+La} = p^l \Big|_{y=Lc+Lm+La} - p^g \Big|_{y=Lc+Lm+La} \quad , \quad (27)$$

which equals a fixed saturation as boundary condition. In the literature the saturation at the boundary is sometimes assumed to be unity[25], which is not very realistic for the hydrophobic GDL since produced CO_2 leaves the GDL through the channel in the gas phase.

Our model includes crossover of methanol and water through the membrane. Due to the high liquid volume fraction, we assume that water transport from anode to the membrane is determined by the liquid phase, i.e., for water the boundary flux into the membrane reads

$$J_{\text{H}_2\text{O}}\big|_{y=L_c+L_m} = \alpha_w (\lambda - 22) , \quad (28)$$

where 22 is the equivalent lambda for the liquid phase. α_w is an empirical parameter describing the water exchange between membrane and catalyst layer.

Since we consider only the gas phase at the cathode side, the boundary flux for water between cathode and membrane reads

$$J_{\text{H}_2\text{O}}\big|_{y=L_c} = \alpha_w (\lambda_{\text{eq}} - \lambda) , \quad (29)$$

where λ_{eq} is a temperature-dependent equivalent lambda for the gas phase at the last CL compartment, which has been fitted using data from Neubrand[26].

For methanol, we apply similar boundary conditions at the membrane, i.e., on the anode side

$$J_{\text{CH}_3\text{OH}}\big|_{y=L_c+L_m} = \alpha_m (c_{\text{CH}_3\text{OH}}^{\text{mem}} - c_{\text{CH}_3\text{OH}}^l) . \quad (30)$$

At the boundary between membrane and cathode we apply Henry's law,

$$J_{\text{CH}_3\text{OH}}\big|_{y=L_c} = \alpha_m (H p_{\text{CH}_3\text{OH}}^g - c_{\text{CH}_3\text{OH}}^{\text{mem}}) . \quad (31)$$

We require continuity of all fluxes at both membrane boundaries.

At the GDL boundary to the cathode channel, the Dirichlet boundary condition is

$$p_i^g \Big|_{y=0} = p_i^{\text{in}} \quad . \quad (32)$$

2.4. Current-voltage relations

We use a physical model[14] which does not require the Nernst equation to calculate the relation between cell voltage and current density. The cell voltage is given by the potential difference between the electrodes,

$$E(i) = \phi_{\text{elde,ca}}(i) - \phi_{\text{elde,an}}(i) \quad . \quad (33)$$

This potential difference is determined by the potential steps between electrode and electrolyte,

$$\Delta\phi_{\text{an}}(y) = \phi_{\text{elde,an}} - \phi_{\text{elyt,an}}(y) \quad , \quad (34)$$

$$\Delta\phi_{\text{ca}}(y) = \phi_{\text{elde,ca}} - \phi_{\text{elyt,ca}}(y) \quad , \quad (35)$$

which in turn follow from electrochemical thermodynamics and kinetics (Section 2.5), and a potential drop due to the resistance of the electrolyte. Combining the continuity equation and Ohm's law yields the governing equation for the potential steps within the porous electrodes,

$$\frac{\partial}{\partial y} \left(\sigma_{\text{mem}} f_{\sigma} \frac{\partial \Delta\phi}{\partial y} \right) = -(i_{\text{F}}^{\text{V}} + i_{\text{dl}}^{\text{V}}) \quad , \quad (36)$$

where i_{F}^{V} is the volumetric Faradaic current due to charge-transfer reactions (cf. Sec. 2.5.2.),

$$i_{\text{F}}^{\text{V}} = F \left(\sum_m \dot{s}_{\text{electron,m}} A_m^{\text{V}} + \sum_n \dot{s}_{\text{electron,n}} l_n^{\text{V}} \right) \quad , \quad (37)$$

and i_{dl}^V is the current due to double layer charging/discharging

$$i_{dl}^V(t) = A_{dl}^V C_{dl} \frac{\partial \Delta \phi}{\partial t} . \quad (38)$$

Within the membrane, there are no source terms, i.e., the continuity equation for the electrolyte potential reads

$$\frac{\partial}{\partial y} \left(\sigma_{mem} \frac{\partial \phi_{elyt}}{\partial y} \right) = 0 . \quad (39)$$

The overpotentials of the anode, cathode and electrolyte are defined as the deviation from the respective potentials at OCV,

$$\eta_{an} = \Delta \phi_{an}^{OCV} - \Delta \phi_{an} , \quad (40)$$

$$\eta_{ca} = -(\Delta \phi_{ca}^{OCV} - \Delta \phi_{ca}) , \quad (41)$$

$$\eta_{el} = \left(\phi_{elyte}^{OCV} \Big|_{y=Lc} - \phi_{elyte}^{OCV} \Big|_{y=Lc+Lm} \right) - \left(\phi_{elyte} \Big|_{y=Lc} - \phi_{elyte} \Big|_{y=Lc+Lm} \right) = \left(\phi_{elyte} \Big|_{y=Lc} - \phi_{elyte} \Big|_{y=Lc+Lm} \right) \quad (42)$$

Note, that the overpotentials have been defined such that their sign under normal operating conditions is positive, to allow for easier comparison.

2.5. Electrochemistry

2.5.1. Reaction kinetics

The production rates of all species are calculated based on the rate equations

$$\dot{s}_i = \sum_m \nu_{i,m} \left(k_{f,m} \prod_{j,educts} a_j^{\nu_{j,m}} - k_{r,m} \prod_{j,products} a_j^{\nu_{j,m}} \right) , \quad (43)$$

where $\nu_{i,m}$ is the stoichiometric factor of species i in reaction m .

For all reactions we consider thermodynamically consistent forward and backward reaction kinetics.

The kinetics of the forward reaction is given by the Arrhenius equation

$$k_f = k_f^0 \exp\left(-\frac{E_f^{\text{act}}}{RT}\right) \exp\left(-\alpha \frac{zF}{RT} \Delta\phi\right) \quad (44)$$

whereas the kinetics of the backward reaction is determined by the thermodynamic consistency equations

$$E_r^{\text{act}} = E_f^{\text{act}} - \Delta H \quad (45)$$

$$k_r^0 = k_f^0 \exp\left(-\frac{\Delta S}{R}\right) \quad (46)$$

The preexponential factor k_f^0 is given by the attempt frequency $\frac{k_B T}{h}$.

Eq. (45) and (46) can also be combined to

$$k_r' = k_f' \exp\left(\frac{\Delta G}{RT}\right), \quad (47)$$

where ΔG is the Gibb's energy of reaction.

The coverages of surface species are calculated based on the production rates as

$$\frac{\partial \theta_i}{\partial t} = \frac{\sigma_i}{\Gamma_k} \dot{s}_i \quad (48)$$

where Γ_k is the site density of surface k and σ_i is the number of sites occupied per surface species.

With this approach quasi irreversibility for certain reactions naturally occurs due to the thermodynamics of the involved species. In case of a single electrochemical reaction, equations (43)-(46) would yield the Nernst equation. In case of multiple electrochemical and chemical reactions, as present in DMFCs, this generalized framework allows to account for effects such as mixed-potential formation, CO poisoning, etc.

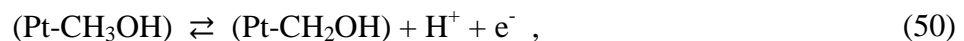
2.5.2. Reaction mechanism

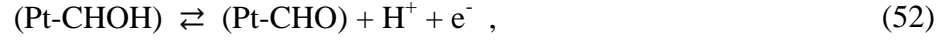
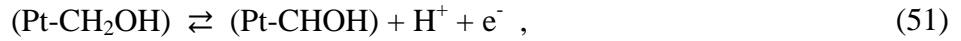
The electrochemical reactions occurring in the CLs are described by elementary kinetics using the thermodynamically consistent approach described above. The oxidation of methanol (MOR) is a complex multi-step process. In literature different possible pathways are proposed. Here we restrict ourselves to one of these pathways, considering the most stable intermediate species based on DFT calculations published by Ferrin et al.[27].

First, methanol adsorbs on the platinum surface



followed by four oxidation steps up to adsorbed CO, which is the most stable intermediate species, leading to a strong CO poisoning of the catalyst.





In order to remove the CO from the platinum surface, we assume the following bi-functional mechanism.

Water can form adsorbed hydroxyl on the ruthenium surface according to



This hydroxyl can subsequently react at the three-phase boundary with the CO adsorbed on platinum to form CO₂



The main mechanism at the cathode side is the oxygen reduction reaction (ORR), which is described by an elementary step mechanism based on DFT calculations[28,29]. However, in order to reduce the complexity when taking into account ORR and MOR at the cathode side, again we consider only one of the possible ORR pathways. This pathway is dominating the

ORR at the potentials relevant for DMFC[29]. Furthermore, we consider the Eley-Rideal reaction steps only, since they have been shown to be the dominant pathway[29].

In the first step oxygen adsorbs on the surface



followed by the dissociation of the oxygen molecule,



Two reduction steps lead to adsorbed water, which in the final step desorbs from the platinum surface



Due to methanol crossover through the membrane, methanol oxidation occurs not only at the anode, but also at the cathode CL. The first steps leading to the CO poisoning are similar to the anode side (49)-(53), so we include these identical reactions also at the cathode.

However, as no ruthenium is present at the cathode, the adsorbed CO has to be removed by a different mechanism, the so called oxygen bleeding using the adsorbed oxygen on the platinum surface, which we include as



The kinetics and thermodynamics used for the ORR is based on the work of Eberle and Horstmann [29], only the kinetics of (58) and (59) and the enthalpy of (Pt-HO) have been adjusted based on the impedance measurements described below. Even though there exist some DFT studies for the MOR on PtRu, the resulting activation energies depend on the method and the conditions considered. Therefore, the parameters for the MOR have been fitted based on the polarization and impedance measurements described in the next section, in order to get a good agreement with the experimental data. The parameters used in this simulation can be found in Table 1 and Table 2.

The reaction kinetics is evaluated in the CANTERA software developed by Goodwin and coworkers [30], which is coupled with our in-house software DENIS as described in the next section.

Table 1. Kinetic parameters for the reactions (49)-(61)

Reaction	$E_f^{\text{act}} / \text{kJ mol}^{-1}$	α
$\text{CH}_3\text{OH} + (\text{Pt}) \rightleftharpoons (\text{Pt-CH}_3\text{OH})$	$48.0 + 25.0 \cdot \theta_{\text{CO}}$	-
$(\text{Pt-CH}_3\text{OH}) \rightleftharpoons (\text{Pt-CH}_2\text{OH}) + \text{H}^+ + \text{e}^-$	0.0	0.5
$(\text{Pt-CH}_2\text{OH}) \rightleftharpoons (\text{Pt-CHOH}) + \text{H}^+ + \text{e}^-$	5.2	0.5
$(\text{Pt-CHOH}) \rightleftharpoons (\text{Pt-CHO}) + \text{H}^+ + \text{e}^-$	37.0	0.5

$(\text{Pt-CHO}) \rightleftharpoons (\text{Pt-CO}) + \text{H}^+ + \text{e}^-$	48.0	0.5
$\text{H}_2\text{O} + (\text{Ru}) \rightleftharpoons (\text{Ru-OH}) + \text{H}^+ + \text{e}^-$	143.0	0.9
$(\text{Pt-CO}) + (\text{Ru-OH}) \rightleftharpoons \text{CO}_2 + \text{H}^+ + \text{e}^- + (\text{Pt}) + (\text{Ru})$	134.0	0.24
$\text{O}_2 + 2 (\text{Pt}) \rightleftharpoons (\text{Pt-O}_2)$	0.0 [29]	-
$(\text{Pt-O}_2) \rightleftharpoons 2 (\text{Pt-O})$	65.61 [29]	-
$(\text{Pt-O}) + \text{H}^+ + \text{e}^- \rightleftharpoons (\text{Pt-HO})$	33.0	0.46 [29]
$(\text{Pt-HO}) + \text{H}^+ + \text{e}^- \rightleftharpoons (\text{Pt-H}_2\text{O})$	13.01	0.54
$(\text{Pt-H}_2\text{O}) \rightleftharpoons \text{H}_2\text{O} + (\text{Pt})$	0.0 [29]	-
$(\text{Pt-CO}) + (\text{Pt-O}) \rightleftharpoons \text{CO}_2 + 2 (\text{Pt})$	14.5	-

Table 2. Thermodynamic parameters

Species	Molar Gibbs energy $G / \text{kJ mol}^{-1}$
(Pt)	0.0 [29]
(Pt-O ₂)	-234.03 [29]
(Pt-O)	-199.51 [29]
(Pt-HO)	-295.18
(Pt-H ₂ O)	-354.52 [29]
(Pt-CH ₃ OH)	-354.93
(Pt-CH ₂ OH)	-297.47
(Pt-CHOH)	-250.22
(Pt-CHO)	-233.84
(Pt-CO)	-248.58
(Ru-OH)	-260.26

2.6. Simulation methodology

The model presented in this paper is mathematically represented by a differential-algebraic equation (DAE) system that describes the mass and charge transport as well as the electrochemistry of the DMFC as described in the previous sections.

The model was implemented into the in-house software package DENIS (detailed electrochemistry and numerical impedance simulation) [14,15]. DENIS includes various models for batteries and fuel cells such as lithium-sulfur (Li-S) cells, lithium-oxygen (Li-O) cells, solid oxide fuel cells (SOFC), polymer electrolyte membrane fuel cells (PEMFC) and, based on the model presented in this manuscript, also DMFC. In order to evaluate the chemical source terms for the reactions described in Sec. 2.5 we use the software CANTERA developed by Goodwin and co-workers [30]. CANTERA is an open-source software written in C++ and allows to define arbitrary reaction mechanisms and species in an ASCII input file, which enables a convenient implementation of complex reaction systems without any modification of the source code itself. CANTERA is coupled to our in-house software DENIS (written in C/C++), making the full CANTERA functionality available during DENIS runtime.

In the presented DMFC model, the computational domain is spatially discretized using the finite-volume method in 1D through the MEA. The numbers of control volumes is 15 in the cathode, 9 in the membrane and 10 in the anode domain.

The DAE system is numerically integrated using the fully implicit solver LIMEX [31, 32]. The time discretization in LIMEX is based on the elementary linearly implicit Euler discretization and allows for adaptive time step size. This is a very important feature especially for the impedance simulations which have to capture processes over a large range of time scales.

3. EXPERIMENTAL

This section briefly describes the experimental measurements used for model validation, consisting of galvanostatic polarization curve measurements, Electrochemical Impedance

Spectroscopy (EIS), methanol crossover measurements, Linear Sweep Voltammetry (LSV), and current interruption (CI).

The experimental setup for the single cell DMFC characterization has been previously described in [4,5]. The single cell DMFC of 25 cm² active area was manufactured by IRD Fuel Cells A/S. Nafion[®] 115 is used as membrane. Anode catalyst loading is 1.8 mg cm⁻² (PtRu) and cathode catalyst loading (Pt) is 1.2 mg cm⁻². Both anode and cathode diffusion layers are SGL35DC and the reactants are fed through a triple serpentine graphite flow field.

The polarization curves shown here are composed of nine single measurement points collected following one-way curves with increasing current (Table 3). Each single acquisition point was performed at constant current, measuring voltage and current at 0.5 Hz frequency for 600 s. After this time period impedance spectra were recorded with an Autolab PGSTAT 30[®] provided with a frequency response analysis module. The impedances were measured under galvanostatic control and the amplitude of the sinusoidal current signal was adjusted so that the potential amplitude does not exceed 10 mV. Excitation frequency was varied between 10 kHz and 50 mHz with a logarithmic distribution. The obtained experimental values were processed by a retrospective use of Kramers–Kronig relations [33] in order to verify the validity of the measurements. The impedance values that did not satisfy such relations were considered not meaningful. As a proxy for methanol crossover, CO₂ measurements are performed at the cathode exhaust with a Vaisala sensor GMP70 (uncertainty 50 ± 2% ppm) in a vessel of 0.5 dm³ volume provided with a liquid-gas gravity separator and a thermocouple [34]. The CO₂ crossover through the membrane is negligible as previously shown by one of the authors [35]. Therefore, assuming a complete methanol oxidation at cathode side, methanol crossover is equal to CO₂ flow rate at cathode outlet subtracted by CO₂ flow rate at cathode inlet, due to ambient concentration. Linear Sweep Voltammetry (LSV) was performed to estimate the magnitude of the internal short circuit current [36], calculated from

the inverse of the slope in the linear region between 0.25 V and 0.55 V. During this measurement hydrogen was supplied to the anode (3.5 Nml min⁻¹) and 80°C saturated nitrogen was supplied to the cathode (0.6 Nl min⁻¹). The cathode potential over the anode was increased from 0.085 V up to 0.55 V with a speed rate of 1 mV s⁻¹, in order to avoid current peaks and achieve the equilibrium between hydrogen crossover and oxidation. The resulting membrane electric resistance is equal to 1.1 kΩ cm² (cf. Fig. 1), leading to a short circuit current in OCV of about 0.616 mA cm⁻².

Moreover, in order to study the dynamic evolution of cathode potential during the change between continuous operation and OCV, a specific current interruption test was performed. The test consists of 10 minutes of continuous operation followed by few minutes of OCV, until voltage reached a steady-state value.

Table 3. Investigated operating conditions.

Temperature	°C	75
Methanol concentration	mol/l	1 / 2
Anode mass flow	g min ⁻¹	3.86 ($\lambda = 6$ at 0.25 A cm ⁻² , 1 M)
Cathode airflow	Nl min ⁻¹	0.336 ($\lambda = 6$ at 0.25 A cm ⁻² , T _{sat} = 30°C)
Current density	A cm ⁻²	0.01/0.05/0.1/0.15/0.2/0.25/0.3/0.35/0.4

4. MODEL RESULTS

4.1 Model validation

The model was parameterized and validated with respect to the experimental measurements described in Sec. 3, i.e., polarization curves, impedance spectra and methanol crossover measurements, in order to ensure that all important processes are correctly described by the model. Especially the electrochemical impedance spectra are very sensitive to the kinetics of the oxygen reduction and the methanol oxidation reaction, allowing to determine the kinetics of the rate determining steps. To simulate impedance spectra, we use a potential step and current relaxation method[37]. Fig. 2 exemplarily shows the effect of the kinetics of CO oxidation, water activation and HO-reduction on the impedance spectra at 0.05A cm^{-2} . The low frequency arc as well as the inductive loop are attributed to the bifunctional mechanism of the methanol oxidation while the high frequency peak is related to the ORR at the cathode.

All simulations shown in the following were carried out with the identical parameter set (Tables 1, 2 and 4), demonstrating the effectiveness of the model in the understanding of DMFC operation.

Table 4. Model parameters.

Parameter	Symbol	Value	Ref.
Temperature	T	75 °C	measured
Thickness GDL cathode	$L_{GDL,Ca}$	350 μm	MEA data sheets
Thickness CL cathode	$L_{CL,Ca}$	30 μm	MEA data sheets
Thickness GDL anode	$L_{GDL,An}$	350 μm	MEA data sheets

Thickness CL anode	$L_{CL,An}$	40 μ m	MEA data sheets
Thickness membrane	L_M	127 μ m	MEA data sheets
Porosity electrodes	ε	0.75	assumed
Platinum ECSA anode	$A_{Pt,An}^V$	$7.5 \cdot 10^6 \text{ m}^2 \text{ m}^{-3}$	assumed
Ruthenium ECSA anode	$A_{Ru,An}^V$	$7.5 \cdot 10^6 \text{ m}^2 \text{ m}^{-3}$	assumed
Triple phase boundary length anode	l_{An}^V	$6 \cdot 10^{11} \text{ m m}^{-3}$	assumed
Platinum ECSA cathode	$A_{Pt,Ca}^V$	$1.0 \cdot 10^7 \text{ m}^2 \text{ m}^{-3}$	measured
Double layer capacitance anode	$C_{dl,An}$	$5 \cdot 10^7 \text{ F m}^{-3}$	fitted
Double layer capacitance cathode	$C_{dl,Ca}$	$2 \cdot 10^7 \text{ F m}^{-3}$	fitted
Site density platinum	Γ_{Pt}	$2.5 \cdot 10^{-5} \text{ mol m}^{-2}$	[38]
Site density ruthenium	Γ_{Ru}	$2.71 \cdot 10^{-5} \text{ mol m}^{-2}$	[39]
Equivalent weight of membrane	EW	1100 g eq $^{-1}$	[22]
Diffusion coefficient methanol in membrane	$D_{CH_3OH}^{mem}$	$9.46 \cdot 10^{-10} \text{ m}^2 \text{ s}^{-1}$	[10]
Diffusion coefficient methanol in liquid phase	$D_{CH_3OH}^l$	$2.8 \cdot 10^{-9} \text{ m}^2 \text{ s}^{-1}$	[40]
Partial molar volume methanol	V_{CH_3OH}	$4.0 \cdot 10^{-5} \text{ m}^3 \text{ mol}^{-1}$	[41]
Water exchange coefficient	α_w	$2 \cdot 10^{-2} \text{ mol m}^{-2} \text{ s}^{-1}$	assumed
Methanol exchange	α_m	$2 \cdot 10^{-6} \text{ mol m}^{-2} \text{ s}^{-1}$	fitted

coefficient			
Henry constant Methanol	H	$2.27 \cdot \exp(5200(1/T - 1/298.15)) \text{ mol m}^{-3} \text{ Pa}^{-1}$	[42]

Fig. 3 shows experimental and simulated polarization curves for cells operated at 1M and 2M methanol concentrations. At low current densities, the cell voltage is slightly lower for 2M due to the higher methanol crossover and the consequential mixed potential at the cathode. However, at high current densities a mass transport limitation sets in, leading to a stronger decrease of the cell voltage at 1M. This behavior can be fully reproduced by the simulations.

Fig. 4 shows experimental and simulated methanol crossover rates for both fuel concentrations. Methanol crossover decreases almost linearly with current density in both cases¹. Again, the simulation reproduces the linear behavior.

Fig. 5 and Fig. 6 show experimental and simulated impedance spectra for various current densities. Model results reproduce experiments with good accuracy. In the literature only few modeling analyses on DMFC impedance can be found[43-45], but none of them are validated considering both anode and cathode contribution. According to our simulations, the higher frequency arc can be attributed to the cathode and strongly depends on the kinetics of the rate determining step in the ORR, reaction (59), while the lower frequency arc can be assigned to the anode as shown by the parameter variations in Fig. 2. Our model is also able to reproduce the typical inductive behavior of the DMFC at very low frequencies, which is caused by the bifunctional mechanism at the anode side. Furthermore, there is good agreement between

¹ The 2M data show a deviation from linear behavior since the 2M data has been recorded after the 1M data and the initial transitory of the vessel for CO₂ measurement was not finished.

simulated and measured relaxation frequencies (Fig. 6); therefore, the involved major physical phenomena are described accurately by the model.

4.2 Steady-state performance

A reliable model-based prediction of the cell voltage during operation is crucial not only for assessment of the cell performance, but also for predicting the cell degradation since, e.g., platinum dissolution strongly depends on the cathode potential.

Fig. 7 shows the simulated polarization curve at 1M methanol and 75°C together with the simulated overpotential contributions. The voltage drop during polarization is dominated by the anode overpotential, while cathode and electrolyte overpotentials only show a rather small increase with current density. Our simulation predicts an OCV of about 0.93V, which is much lower than the thermodynamic value of 1.21V. This 0.28 V difference is consistent with the experimental values reported in a recent work by the authors [46]. The reason for this difference is the effect of methanol crossover to the cathode which leads to the formation of the so-called mixed potential. This reduction of OCV occurs naturally in our model due to the reversible formulation of all reactions including the methanol oxidation at the cathode side. To demonstrate the effect of the crossover, we run a simulation with the same parameters, but assuming that the membrane has no permeability for methanol. The corresponding cell voltage and overpotentials are also shown in Fig. 7. In this case, the calculated OCV is about 1.2V. However, similar to the behavior in PEMFC the cathode overpotential strongly increases at low current densities due to the sluggish ORR kinetics. Therefore, at intermediate current densities the cell voltage is comparable to the case with crossover. An effect of

crossover is mainly observed at low current densities where the reduction of cell voltage is more pronounced due to the higher crossover.

In the simulation case with methanol crossover, the calculated OCV of 0.93V is still significantly higher than the typical OCV of about 0.7V observed in experiments. The discrepancy can be explained by taking into account the effect of the internal short circuit current, which has been determined by LSV measurements to have a value of about 6.16 A m^{-2} (cf. Sec. 3). The effect of the short circuit is negligibly small under normal operation due to the high membrane electric resistance of $1.1 \text{ k}\Omega \text{ cm}^2$, but it is important for the OCV. The short circuit current is not explicitly included in the model. Nevertheless, we can easily calculate its effect on the OCV. At OCV, the total current density is not zero but equals the short circuit current density (no external load). Thus, the measured OCV is given by $U(i=i_{\text{short-circuit}})$ instead of $U(i=0)$.

As shown in Fig. 7 the model predicts a very strong increase of the anode overpotential at low current densities, due to the fact that already very low current densities lead to a high CO-poisoning of the catalyst surface. Therefore, the low internal short circuit current density is already enough to reduce the OCV from the theoretical value of 0.93V, which is obtained for platinum without CO-poisoning, down to about 0.7V (the voltage obtained from the simulation at 6.16 A m^{-2} is 0.72V). Voltages higher than this value can only be obtained for short time periods, e.g., after current interruption (see below), by temporary reducing the methanol crossover or the CO-poisoning.

4.3 Transient behavior

Our model also allows investigating transient effects. An important issue is the effect of cycling on cell performance and degradation. In fact, DMFC are typically operated with dynamic operating strategies characterized by operation interruption. Therefore, understanding the effect of current interruption is important to predict cell performance and durability. In order to study this effect, we performed a transient simulation switching between different current densities and internal short-circuit current of 6.16A/m^2 (corresponding to going to OCV as discussed above). The resulting simulated cell voltage is shown in Fig. 8(top). The cycling leads to significant transient effects of cell potential especially at OCV. After current interruption the cell voltage increases up to about 0.88V, which is much higher than the steady-state OCV of 0.7V. The maximum voltage as well as the duration of this overshoot depends on the current density before the interruption. Fig. 8(bottom) shows the anode and cathode overpotentials for a single current interruption. As one can see, the main contribution of the overshoot is due to the anode side.

A similar behavior after current interruption has been observed also experimentally (Fig. 9). However, compared to the model the experimentally observed relaxation is slower. To understand this difference, we have to understand the physical origin of the transient behavior.

At the anode, high current densities lead to a reduction of the CO-poisoning due to a faster CO oxidation. Going back to OCV the CO and OH coverages have to relax to their equilibrium values. This leads to an overshoot in anode potential, causing the peak in cell voltage after current interruption. The size and duration of the anode overshoot is strongly dependent on the kinetics of the bifunctional mechanism, i.e., of the CO oxidation and water activation reactions. Fig. 10 shows the effect of the reaction kinetics on the overshoot. Fig. 11 shows the corresponding evolution of the (Pt-CO) and (Ru-OH) coverages.

The change of cathode potential can be attributed to the variation of methanol crossover. At high current densities, most of the methanol is consumed at the anode side, consequently the methanol concentration in the membrane and at the cathode side is low. Going back to OCV, two effects occur. First, the contribution of electro-osmotic drag to methanol crossover vanishes. This leads to an even lower methanol crossover for a short period of time. However, at the same time the methanol concentration at the anode side increases causing an increased methanol diffusion through the membrane, eventually leading to an increase in methanol crossover. Fig. 12 shows the transient behavior of methanol crossover during cycling and after current interruption. As long as the methanol crossover is lower than the equilibrium value at OCV, methanol oxidation at the cathode side is reduced leading to a lower (negative) cathode overpotential, i.e., a potential overshoot (cf. Fig. 12).

In our simulation with methanol standard diffusion coefficient from the literature, this overshoot at the cathode side is relatively short (approx. 100 seconds) and not very pronounced, while in experiments a slower relaxation of potential has been observed as shown in Fig. 9. There are two possibilities explaining this difference. First, in our model we do not consider the micro-porous layer (MPL) at the anode and cathode side. The MPL at the anode can lead to a slower relaxation of the methanol crossover after current interruption, i.e., a longer and higher overshoot of the cathode potential. To illustrate this effect, simulations with exactly the same parameters except for a lower methanol diffusion coefficient through the membrane were performed and the results are also shown in Fig. 12. In this case, the oscillations in methanol crossover and consequently the potential overshoot are strongly increased.

Another mechanism which leads to a decrease of the cathode potential with time is the platinum oxide formation[47]. This mechanism is often discussed in the literature in the context of platinum dissolution, which is affected by Pt-oxide formation[48]. Pt-oxide formation as a reversible degradation mechanism and its effect on the platinum particle growth is currently investigated by the authors and will be published elsewhere.

5. CONCLUSIONS

We have presented a detailed DMFC performance model including two-phase transport for the methanol water mixture, methanol crossover through the membrane and elementary kinetics formulation of the reactions on the catalyst surfaces. This cell model allows not only polarization curve simulations, but also studying the transient behavior of the cell as well as impedance simulations.

The model was validated by means of different experimental methods using one single set of model parameters, demonstrating the reliability of the results. After validation, the effect of methanol crossover and CO poisoning on the cell performance during steady-state and transient operation was studied. Under steady state conditions both mechanisms strongly affect the OCV, leading to a value of about 0.7V.

Furthermore, transient simulations demonstrated that cycling has a significant effect on both cathode and anode overpotentials due to the transient behavior of methanol crossover and CO poisoning. These transient effects are very important when studying potential-dependent reversible and irreversible degradation phenomena, e.g., platinum oxide formation and platinum dissolution. An accurate model for the catalyst degradation of DMFC by means of

platinum particle growth mechanisms coupled to platinum oxide formation is currently under development by the authors and will be presented elsewhere.

ACKNOWLEDGEMENT

The research leading to these results has received funding from the European Union's Seventh Framework Program (FP7/2007-2013) for the Fuel Cells and Hydrogen Joint Technology Initiative under grant agreement n°256776 (FCH-JU project Premium Act) and n°621216 (FCH-JU project Second Act).

WGB and TJ acknowledge support from the Initiative and Networking Fund of the Helmholtz Association.

The authors thank Dr. Birger Horstmann (German Aerospace Center) for fruitful discussions.

NOMENCLATURE

Symbol	Unit	Meaning
A_k^V	$\text{m}^2 \cdot \text{m}^{-3}$	Volume-specific surface area corresponding to reaction k
c_i	$\text{mol} \cdot \text{m}^{-3}$	Concentration of species i in a bulk phase
C_{dl}	$\text{F} \cdot \text{m}^2$	Area-specific double layer capacitance
d_i		Drag coefficient of species i
d_p	m	Average particle diameter
D_i^p	$\text{m}^2 \cdot \text{s}^{-1}$	Diffusion coefficient of species i in phase p
E	V	Cell voltage
EW	$\text{kg} \cdot \text{eq}^{-1}$	Equivalent weight of membrane

E_f^{act}	$\text{J}\cdot\text{mol}^{-1}$	Activation energy of forward and reverse reactions
f_σ		Ratio of ionic conductivity of porous over bulk electrolyte
F	$\text{C}\cdot\text{mol}^{-1}$	Faraday's constant
H	$\text{mol}\cdot\text{m}^{-3}\cdot\text{Pa}$	Henry's constant
i	$\text{A}\cdot\text{m}^{-2}$	Current density
$j_i^{l,\text{diff}}$	$\text{kg}\cdot\text{m}^{-2}\cdot\text{s}^{-1}$	Mass diffusion flux of species i in liquid phase
$j_i^{l,\text{conv}}$	$\text{kg}\cdot\text{m}^{-2}\cdot\text{s}^{-1}$	Mass convection flux of species i in liquid phase
$J_i^{g,\text{diff}}$	$\text{mol}\cdot\text{m}^{-2}\cdot\text{s}^{-1}$	Molar diffusion flux of species i in gas phase
$J_i^{g,\text{conv}}$	$\text{mol}\cdot\text{m}^{-2}\cdot\text{s}^{-1}$	Molar convection flux of species i in gas phase
k^p	m^2	Permeability of phase p
k_{abs}	m^2	Absolute permeability
k_{rel}^p		Relative permeability of phase p
l_n^V	$\text{m}\cdot\text{m}^{-3}$	Volume-specific three-phase boundary length corresponding to reaction n
La	m	Thickness of anode (GDL + CL)
Lc	m	Thickness of cathode (GDL + CL)
Lm	m	Thickness of membrane
M_i	$\text{kg}\cdot\text{mol}^{-1}$	Molar mass of species i
p^c	Pa	Capillary pressure
p^g	Pa	Gas pressure
p_i^g	Pa	Partial pressure of species i in gas phase
p^l	Pa	Liquid pressure
\bar{p}^p	Pa	Pressure of phase p averaged over channel length

R	$\text{J}\cdot\text{K}^{-1}\cdot\text{mol}^{-1}$	Ideal gas constant
s		Liquid saturation
\dot{s}_i^k	$\text{mol}\cdot\text{m}^{-2}\cdot\text{s}^{-1}$ $\text{mol}\cdot\text{m}^{-1}\cdot\text{s}^{-1}$	Chemical production rate of species i in reaction k (in units of m^{-2} for two-phase reactions and m^{-1} for three-phase reactions)
\dot{s}_i^{cond}	$\text{mol}\cdot\text{m}^{-2}\cdot\text{s}^{-1}$	Production rate of species i due to condensation
$\dot{s}_{\text{electron},m}$	$\text{mol}\cdot\text{m}^{-2}\cdot\text{s}^{-1}$ $\text{mol}\cdot\text{m}^{-1}\cdot\text{s}^{-1}$	Electron production rate in reaction m (in units of m^{-2} for two-phase reactions and m^{-1} for three-phase reactions)
t	s	Time
T	K	Temperature
v^{conv}	$\text{m}\cdot\text{s}^{-1}$	Convection velocity in liquid phase
$\bar{V}_{\text{H}_2\text{O}}$	$\text{mol}\cdot\text{m}^{-3}$	Molar volume of water
\bar{V}_{mem}	$\text{mol}\cdot\text{m}^{-3}$	Molar volume of the dry membrane
x_i^p		Mole fraction of species i in phase p
z		Number of electrons transferred in charge-transfer step
α		Symmetry factor of charge transfer reaction
α_w	$\text{mol}\cdot\text{m}^{-2}\cdot\text{s}^{-1}$	Water exchange coefficient
α_m	$\text{mol}\cdot\text{m}^{-2}\cdot\text{s}^{-1}$	Methanol exchange coefficient
Γ_i	$\text{mol}\cdot\text{m}^{-2}$	Site density of surface i
ΔH	$\text{J}\cdot\text{mol}^{-1}$	Reaction enthalpy
ΔS	$\text{J}\cdot\text{K}^{-1}\cdot\text{mol}^{-1}$	Reaction entropy
$\Delta\phi$	V	Electric potential difference between electrode and electrolyte
ε		Porosity
ε_i		Volume fraction of phase i
ϕ	V	Electric potential

μ^g	$\text{kg}\cdot\text{m}^{-1}\cdot\text{s}^{-1}$	Gas-phase viscosity
μ^l	$\text{kg}\cdot\text{m}^{-1}\cdot\text{s}^{-1}$	Liquid-phase viscosity
ρ_i^l	$\text{kg}\cdot\text{m}^{-3}$	Density of species <i>i</i>
σ_{mem}	$\text{S}\cdot\text{m}^{-1}$	membrane conductivity
τ		Tortuosity of porous electrode

REFERENCES

- [1] S.C. Thomas, X. Ren, S. Gottesfeld, P. Zelenay, *Electrochim. Acta* 47 (2002) 3741.
- [2] A.S. Aricò, S. Srinivasan, V. Antonucci, *Fuel Cells* 1 (2001) 133.
- [3] H.-C. Cha, C.-Y. Chen, J.-Y. Shiu, *J. Power Sources* 192 (2009) 451.
- [4] F. Bresciani, A. Casalegno, M. Zago, R. Marchesi, *Fuel Cells* 14 (2014) 386.
- [5] F. Bresciani, C. Rabissi, A. Casalegno, M. Zago, R. Marchesi, *Int. J. Hydrogen Energy* 39 (2014) 21647.
- [6] F. Bresciani, C. Rabissi, M. Zago, P. Gazdzicki, M. Schulze, L. Guetaz, S. Escribano, J.L. Bonde, R. Marchesi, A. Casalegno, *J. Power Sources* 306 (2016) 49.
- [7] Z.H. Wang, C.Y. Wang, *J. Electrochem. Soc.* 150 (2003) A508.
- [8] A. Siebke, W. Schnurnberger, F. Meier, G. Eigenberger, *Fuel Cells* 3 (2003) 37.
- [9] M. Zago, A. Casalegno, F. Bresciani, R. Marchesi, *Int. J. Hydrogen Energy* 39 (2014) 21620.
- [10] D. Gerteisen, *J. Power Sources* 195 (2010) 6719.
- [11] A.A. Kulikovskiy, *Electrochim. Acta* 62 (2012) 185.
- [12] P.A. García-Salaberri, M. Vera, *Energy* 113 (2016) 1265.
- [13] A.A. Kulikovskiy, *Electrochim. Acta* 56 (2011) 9846.
- [14] W.G. Bessler, S. Gewies, M. Vogler, *Electrochim. Acta* 53 (2007) 1782.
- [15] J.P. Neidhardt, D.N. Fronczek, T. Jahnke, T. Danner, B. Horstmann, W.G. Bessler, *J. Electrochem. Soc.* 159 (2012) A1528.

- [16] B. Horstmann, T. Danner, W.G. Bessler, *Energy Environ. Sci.* 6 (2013) 1299.
- [17] M. Laliberte, *J. Chem. Eng. Data* 52 (2007).
- [18] N. Zamel, X. Li, J. Becker, A. Wiegmann, *Int. J. Hydrogen Energy* 36 (2011) 5466.
- [19] J. Bear, *Dynamics of Fluids in Porous Media*, Elsevier, New York, 1972.
- [20] L. Hao, P. Cheng, *Int. J. Heat Mass Transf.* 55 (2012) 133.
- [21] H. Hertz, *Ann. der Phys. und Chemie* 17 (1882) 177.
- [22] A.Z. Weber, J. Newman, *J. Electrochem. Soc.* 151 (2004) A311.
- [23] F. Meier, G. Eigenberger, *Electrochim. Acta* 49 (2004) 1731.
- [24] B.L. García, V. A. Sethuraman, J.W. Weidner, R.E. White, R. Dougal, *J. Fuel Cell Sci. Technol.* 1 (2004) 43.
- [25] W.W. Yang, T.S. Zhao, *J. Power Sources* 188 (2009) 433.
- [26] W. Neubrand, *Modellbildung und Simulation von Elektromembranverfahren*, PhD Thesis, 1999.
- [27] P. Ferrin, A.U. Nilekar, J. Greeley, M. Mavrikakis, J. Rossmeisl, *Surf. Sci.* 602 (2008) 3424.
- [28] J. A. Keith, T. Jacob, *Angew. Chemie* 122 (2010) 9711.
- [29] D. Eberle, B. Horstmann, *Electrochim. Acta* 137 (2014) 714.
- [30] D. G. Goodwin, Cantera, <http://www.cantera.org>, 2001–2005.
- [31] P. Deuflhard, E. Hairer, J. Zugck, *Num. Math.*, 51, (1987) 501.
- [32] R. Ehrig, U. Nowak, L. Oeverdieck, P. Deuflhard, in *High performance scientific and engineering computing. Lecture notes in computational science and engineering*, H.-J. Bungartz, F. Durst, and C. Zenger Editors, p. 233, Springer (1999).
- [33] E. Barsoukov, J.R. Macdonald, eds., *Impedance Spectroscopy: Theory, Experiment, and Applications*, Wiley-Interscience, New York, 2005.
- [34] F. Bresciani, C. Rabissi, M. Zago, R. Marchesi, A. Casalegno, *J. Power Sources* 273 (2015) 680.
- [35] A. Casalegno, C. Santoro, F. Rinaldi, R. Marchesi, *J. Power Sources* 196 (2011) 2669
- [36] H. Wang, X.Z. Yuan, H. Li, *Handbook of PEM Fuel Cell Durability*, Taylor & Francis, Boca Raton, 2011.

- [37] W.G. Bessler, *J. Electrochem. Soc.* 154 (2007) B1186.
- [38] S.P. Devarajan, J.A. Hinojosa Jr., J.F. Weaver, *Surf. Sci.* 602 (2008) 3116.
- [39] M.L. Toebes, *Carbon Nanofibers as Catalyst Support for Noble Metals*, PhD Thesis, 2004.
- [40] K. Scott, P. Argyropoulos, K. Sundmacher, 477 (1999) 97.
- [41] P. Hynčica, L. Hnědkovský, I. Cibulka, *J. Chem. Thermodyn.* 36 (2004) 1095.
- [42] R. Sander, *Compilation of Henry's Law Constants for Inorganic and Organic Species of Potential Importance in Environmental Chemistry*, 1999.
- [43] A.A. Kulikovsky, *Electrochem. Commun.* 24 (2012) 65.
- [44] M. Zago, A. Casalegno, *J. Power Sources* 248 (2014) 1181.
- [45] U. Krewer, M. Christov, T. Vidakovic', K. Sundmacher, *J. Electroanal. Chem.* 589 (2006) 148.
- [46] M. Zago, A. Bisello, A. Baricci, C. Rabissi, E. Brightman, G. Hinds, A. Casalegno, *J. Power Sources* 325 (2016) 714.
- [47] C. Eickes, P. Piela, J. Davey, P. Zelenay, *J. Electrochem. Soc.* 153 (2006) A171.
- [48] R.M. Darling, J.P. Meyers, *J. Electrochem. Soc.* 150 (2003) A1523.

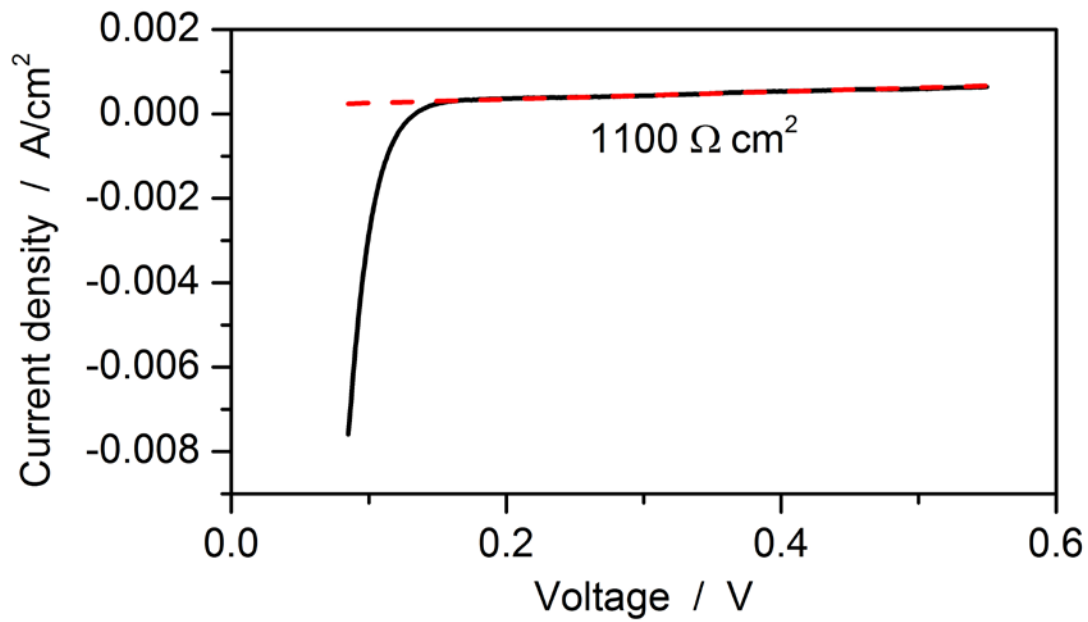
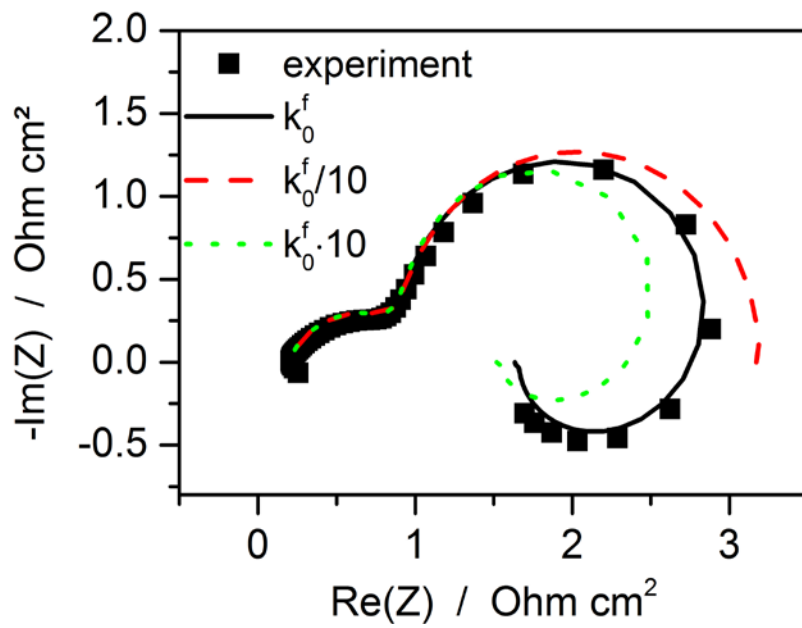


Fig. 1: LSV measurement to determine the short circuit current. The dashed line shows the linear fit leading to a resistance of $1100 \Omega \text{ cm}^2$.



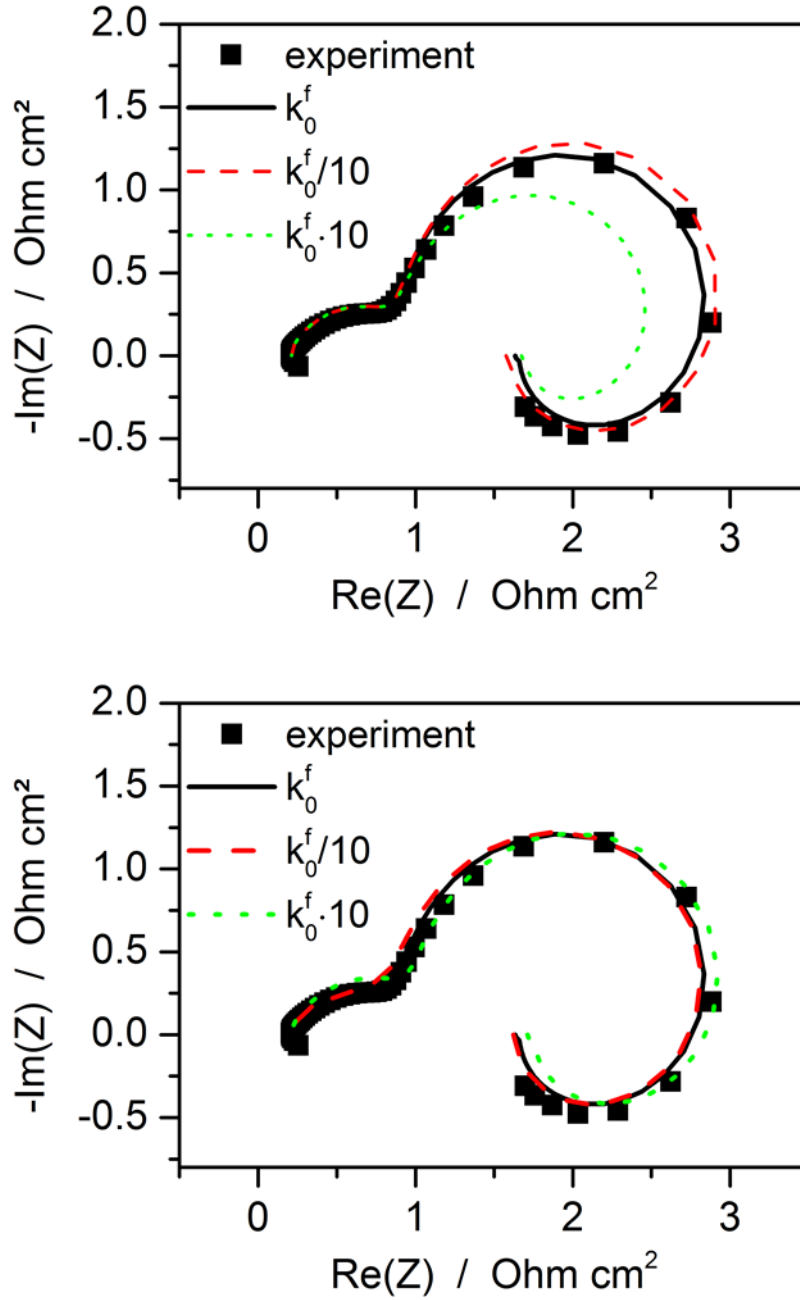


Fig. 2: Effect of the reaction kinetics on the impedance at 0.05 A cm^{-2} . Top: Variation of CO oxidation Eq. (52) kinetics. For sufficiently slow CO oxidation the inductive feature of the impedance vanishes. Middle: Variation of water activation Eq. (51) kinetics. Faster kinetics leads to significantly smaller capacitive and inductive arcs without significant change of the total resistance. Bottom: Variation of (Pt-HO) reduction step Eq. (56) kinetics. Even though the effect on the impedance is quite small, this reaction is the rate determining step of the ORR at cathode potentials relevant for DMFC and strongly affects the cell performance. Variations of the kinetics for this reaction mainly lead to a translation of

the polarization curves. For example, at 0.05 A cm^{-2} the difference between the ten times higher and ten times lower kinetics is about 73mV.

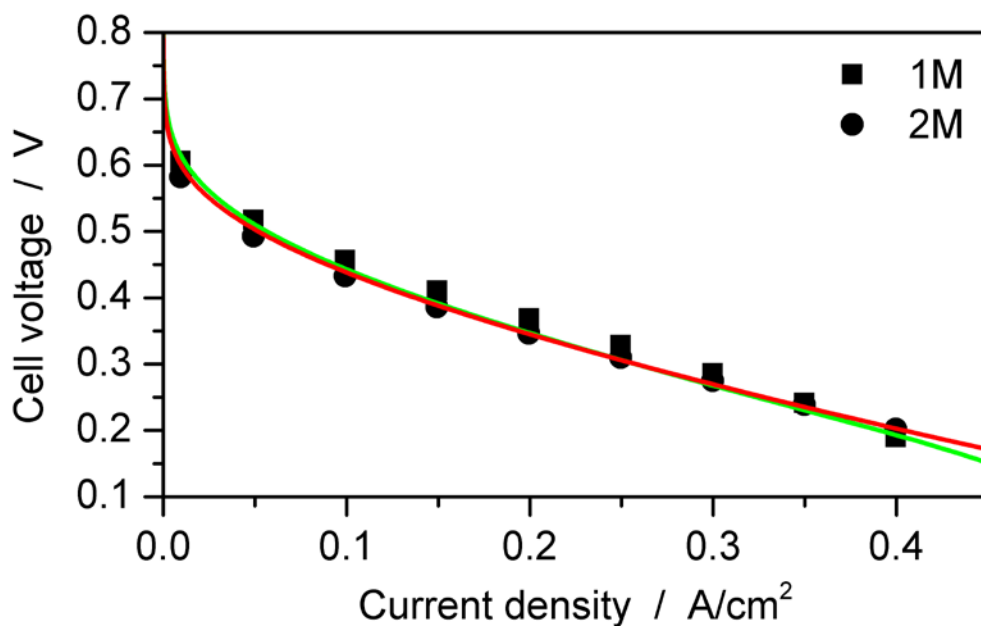


Fig. 3: Polarization curves at 1M and 2M methanol concentration at $T = 348 \text{ K}$. The symbols represent experimental data, the lines corresponding simulations (green 1M, red 2M).

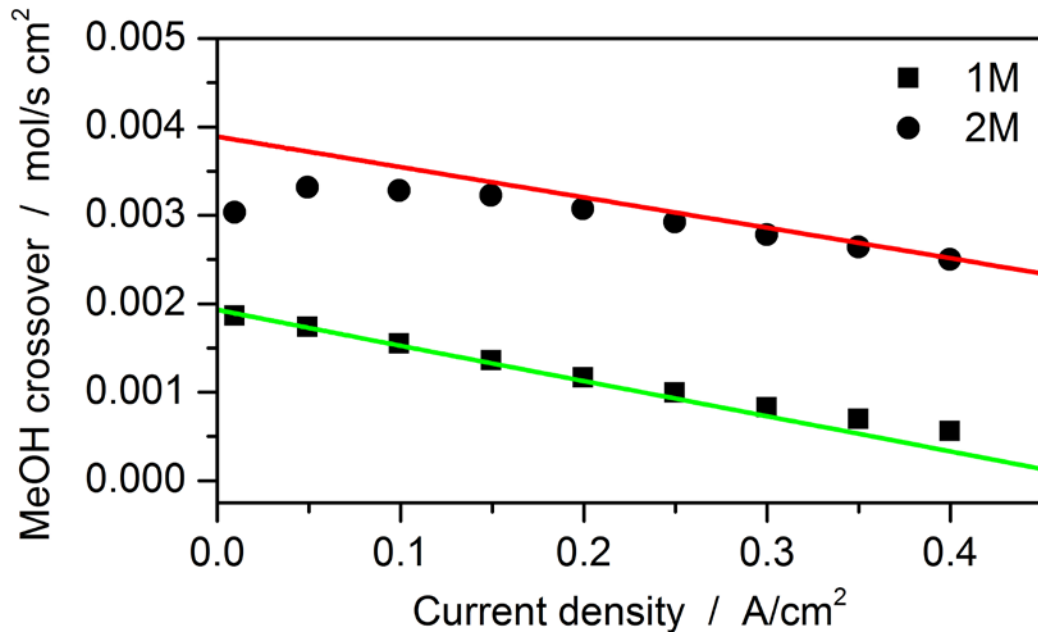


Fig. 4: Comparison of measured and simulated methanol crossover for 1M and 2M methanol concentration. The symbols represent experimental data, the lines corresponding simulations.

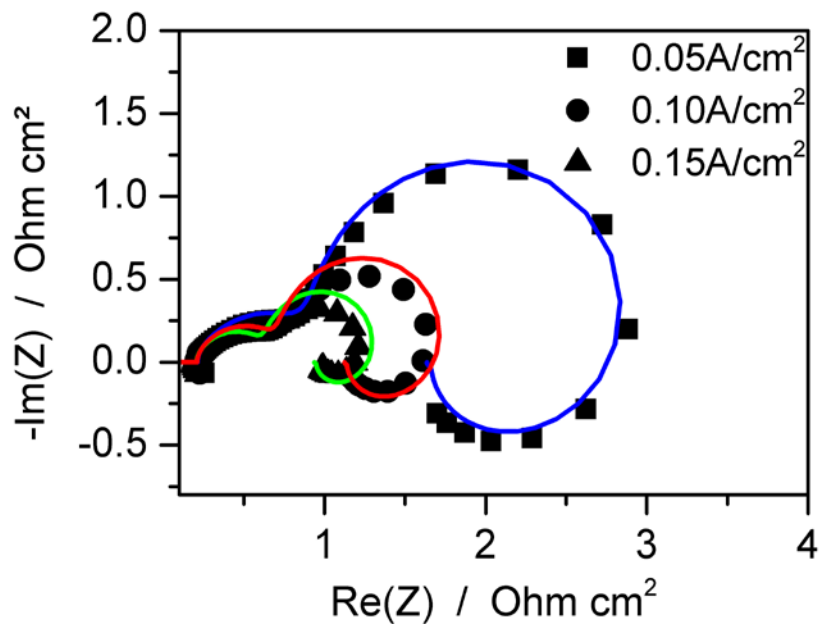


Fig. 5: Nyquist plot of simulated and measured impedance spectra at 1M methanol for various current densities. The symbols represent experimental data, the lines corresponding simulations.

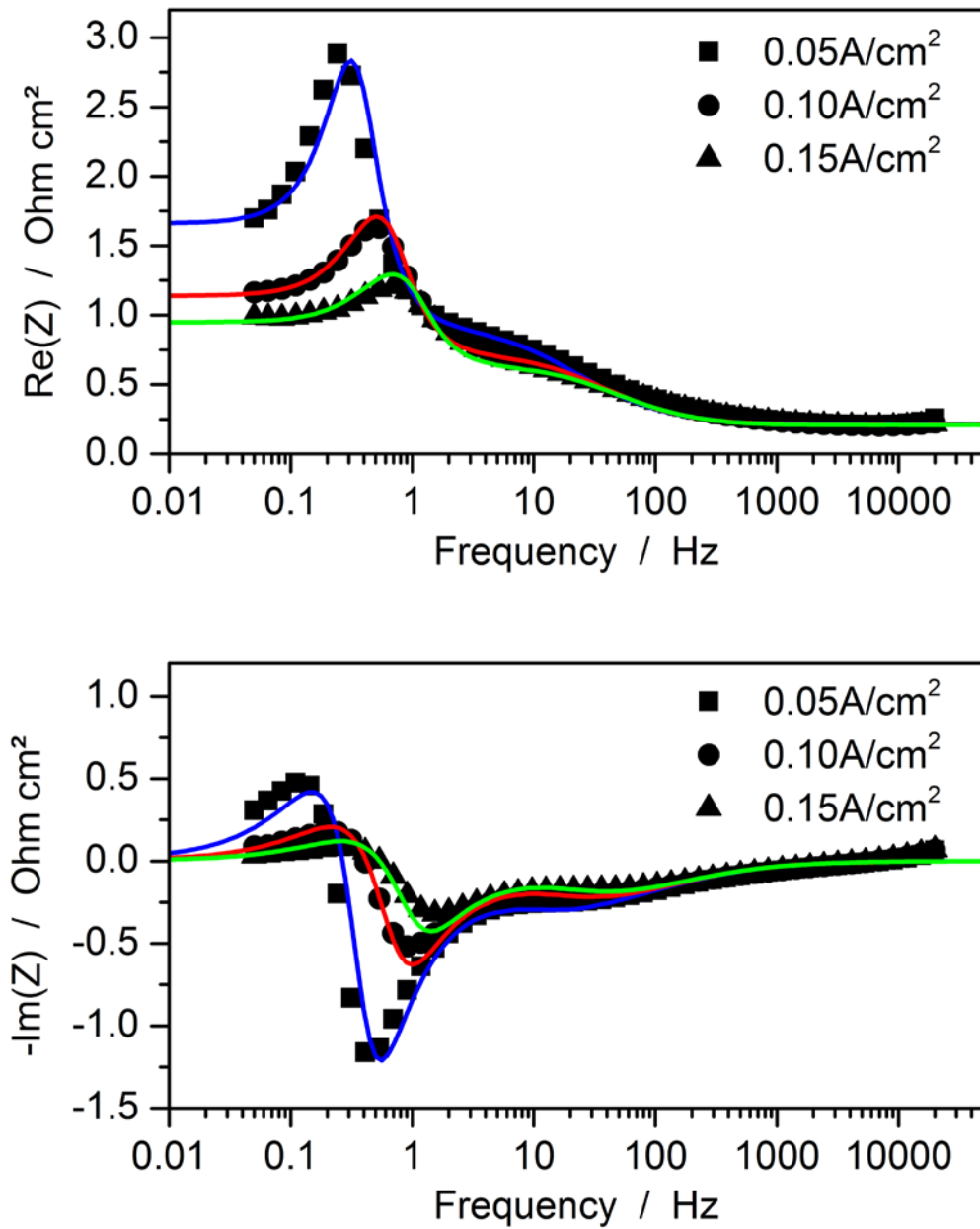


Fig. 6: Real part (top) and imaginary part (bottom) of simulated and measured impedance spectra. The symbols represent experimental data, the lines corresponding simulations. Same data as in Fig. 5.

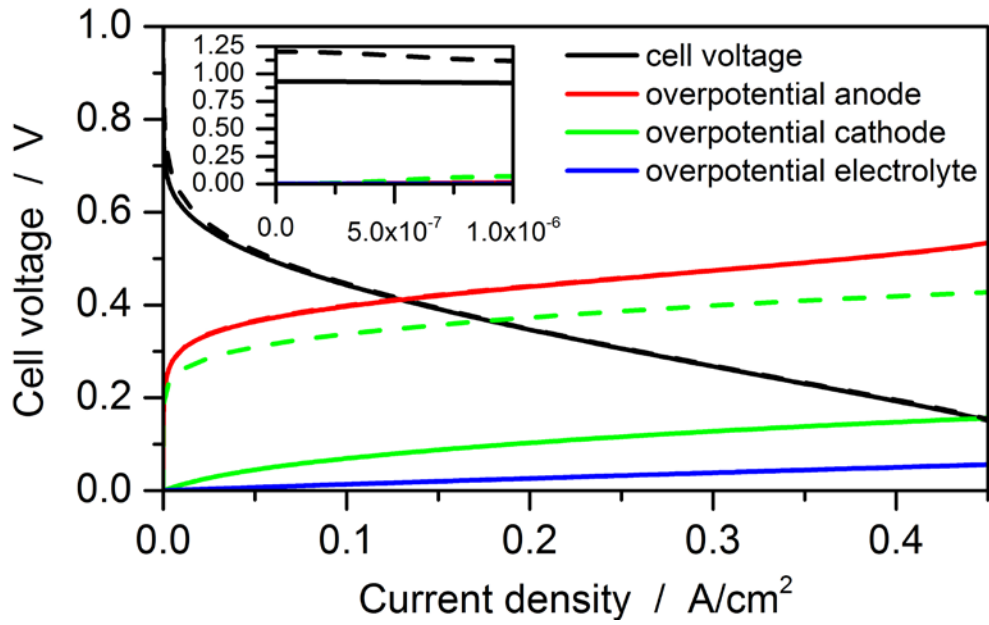
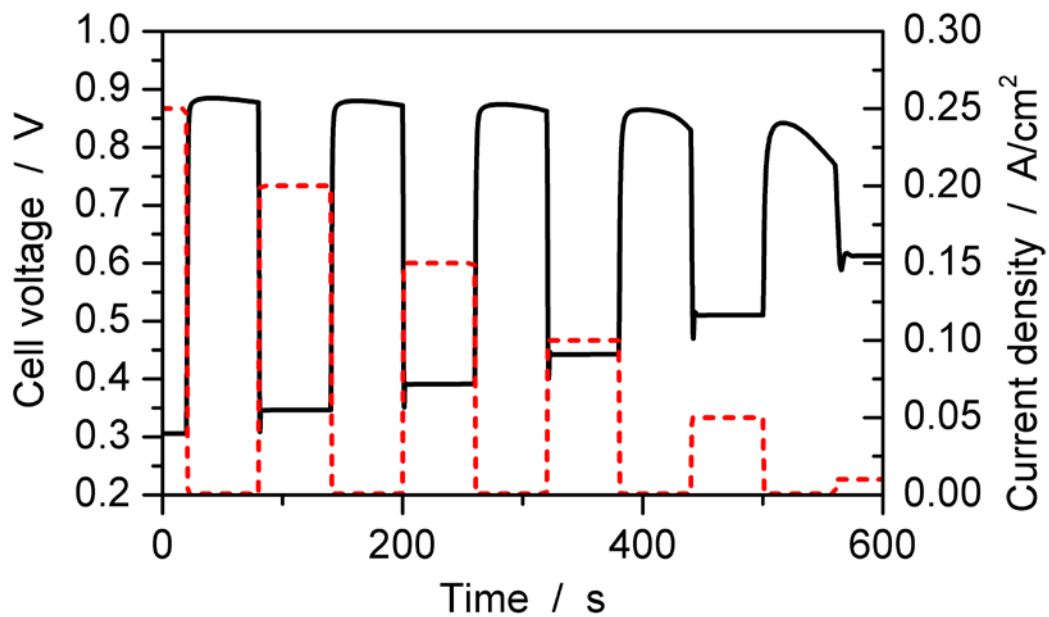


Fig. 7: Simulated polarization curve at 1M with respective overpotentials of anode, cathode and electrolyte. To demonstrate the effect of methanol crossover, the dashed lines correspond to the simulation without methanol permeation through the membrane.



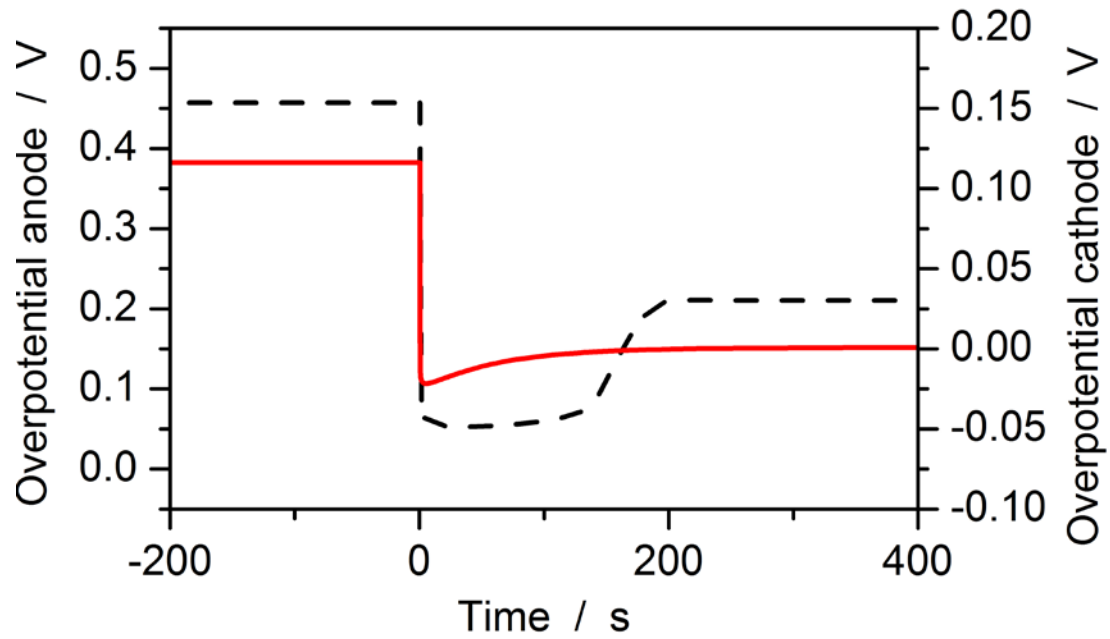


Fig. 8: Top: Simulated cell voltage (solid line) after current interruption at (from left to right) 0.25 A cm^{-2} , 0.2 A cm^{-2} , 0.15 A cm^{-2} , 0.1 A cm^{-2} and 0.05 A cm^{-2} . After 60 seconds under OCV conditions the cell voltage is switched to the next lower current density (dashed line). Bottom: Simulated overpotentials of the cathode (solid line) and the anode (dashed line) after interruption of the current density of 0.25 A cm^{-2} .

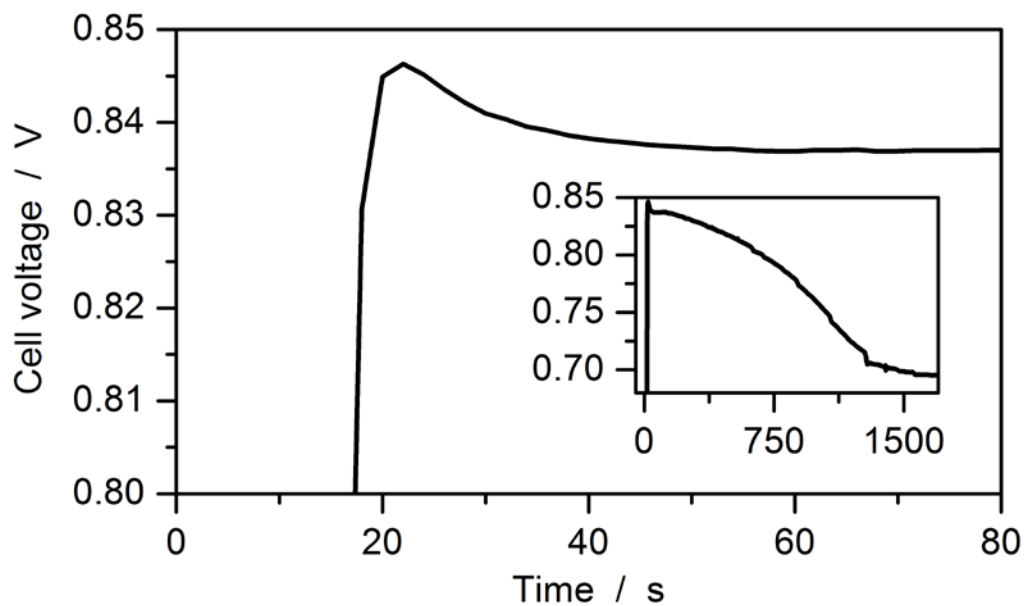


Fig. 9: Current interruption experiment: transient behavior of cell voltage after interruption of the

current density of 0.25 A cm^{-2} .

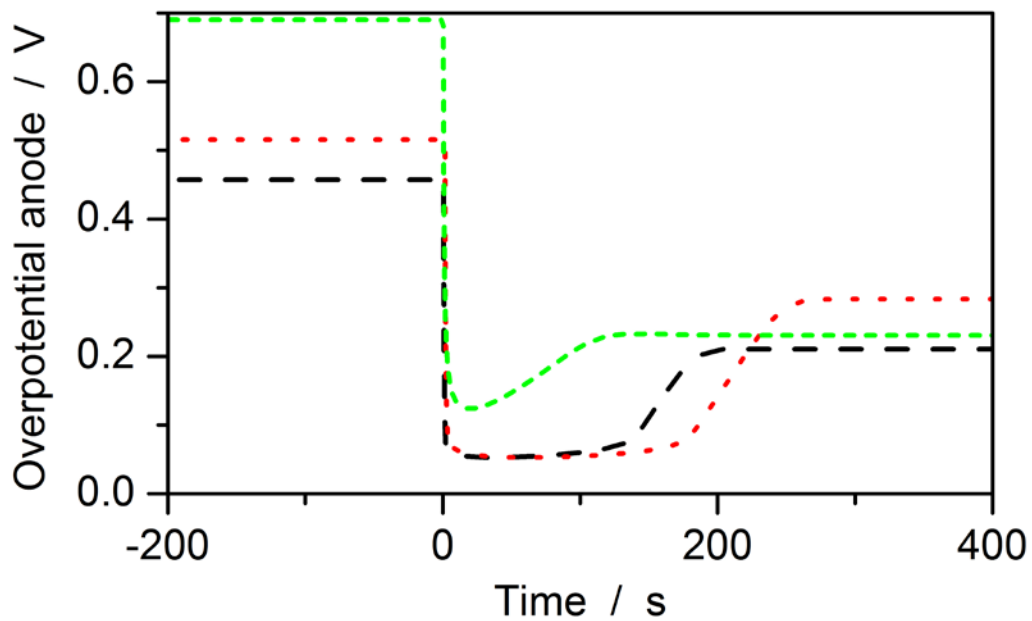


Fig. 10: Effect of the reaction kinetics on the anode overshoot: the red line corresponds to a ten times slower water activation reaction (Eq. (51)) and the green line to a ten times slower CO oxidation reaction (Eq. (52)) compared to the standard parameters (black).

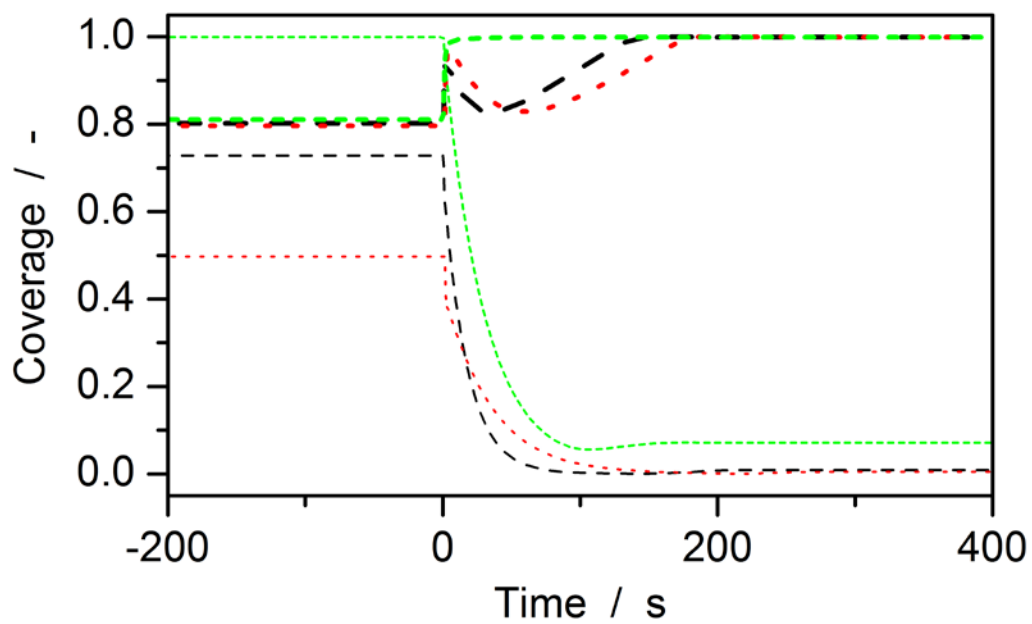


Fig. 11: Simulated evolution of the (Pt-CO) (thick lines) and (Ru-OH) (thin lines) coverages during current interruption for the different kinetics corresponding to Fig. 10.

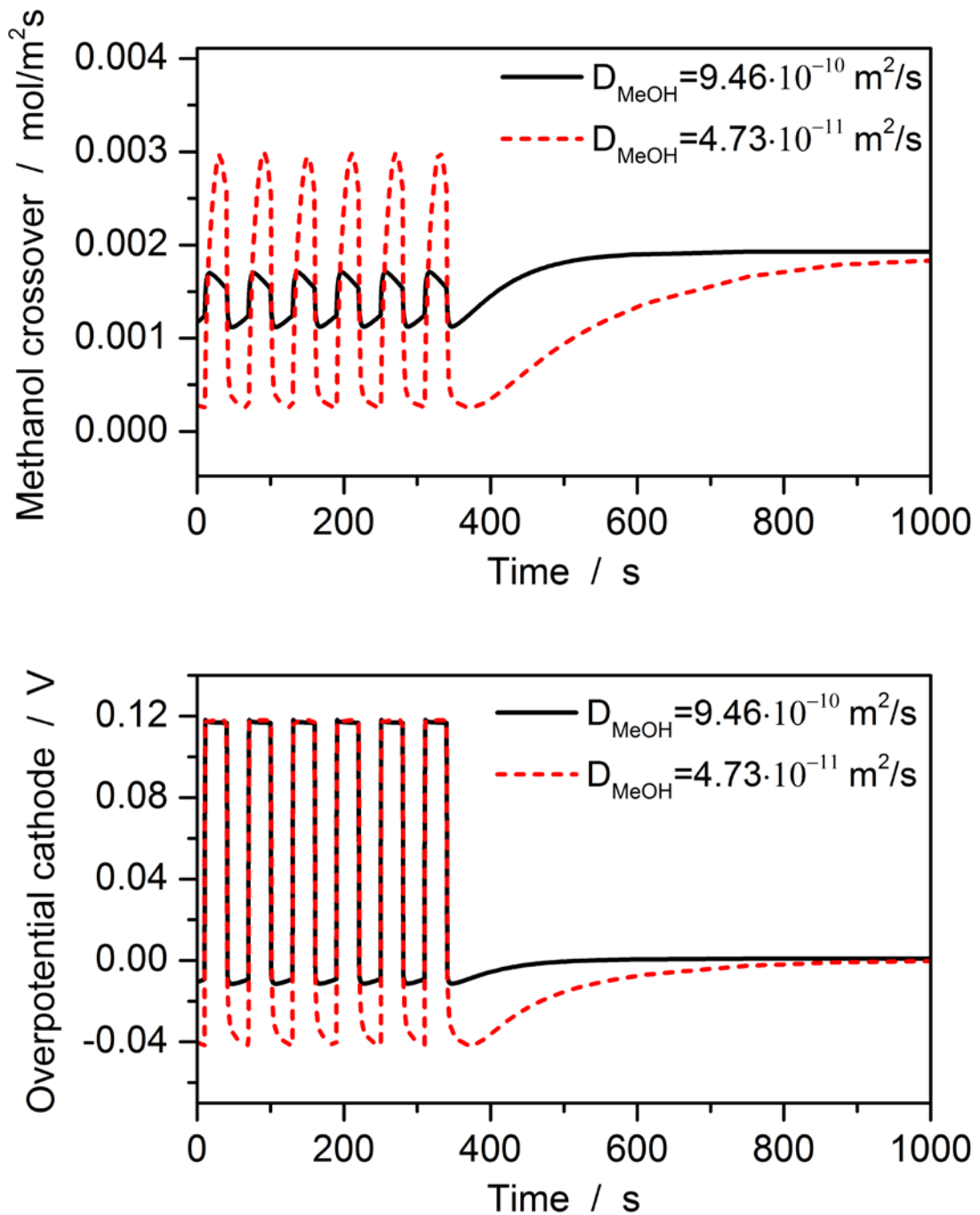


Fig. 12: Simulated methanol crossover (top) and cathode overpotential (bottom) during cycling between 0.25 A cm^{-2} and short circuit current and after current interruption for two different methanol diffusion coefficients within the membrane.